ISIJ International, Vol. 56 (2016), No. 4, pp. 574–583

In-situ Study of Crystallisation Behaviour of $CaO–SiO_2–Na_2O–B_2O_3–TiO_2–Al_2O_3–MgO–Li_2O$ Fluorine-free Mould Fluxes with Different CaO/SiO_2 Ratios

Jian YANG,[1)] Jianqiang ZHANG,[1)]* Yasushi SASAKI,[1)] Oleg OSTROVSKI,[1)] Chen ZHANG,[2)] Dexiang CAI[2)] and Yoshiaki KASHIWAYA[3)]

1) School of Materials Science and Engineering, The University of New South Wales, Sydney, NSW 2052 Australia.
2) Baosteel Group Corporation Research Institute, Baoshan District, Shanghai, 201900 China.
3) Department of Energy Science and Technology, Kyoto University, Yoshida-Honmachi, Sakyo-ku, Kyoto, 606-8501 Japan.

(*Received on October 19, 2015; accepted on November 27, 2015*)

The increasing environmental concern for the fluorine emission in steel continuous casting makes the development of fluorine-free mould fluxes imperative. The main challenge in the development of fluorine-free mould fluxes is controlling heat transfer rate which is closely related to the crystallisation behaviour of mould fluxes. In this study, the crystallisation behaviour of $CaO–SiO_2–Na_2O–B_2O_3–TiO_2–Al_2O_3–MgO–Li_2O$ fluorine-free mould fluxes with CaO/SiO_2 mass ratios from 0.9 to 1.2 was examined using single hot thermocouple technique (SHTT) and double hot thermocouple technique (DHTT). Continuous cooling transformation (CCT) and time-temperature transformation (TTT) diagrams developed using SHTT showed that the crystallisation temperature increased and the incubation time decreased with the increase of CaO/SiO_2 ratio. DHTT was used to simulate the temperature gradient between copper mould and strand in steel continuous casting. Analysis of the crystallinity evolution in the simulated temperature field showed an increased crystallinity of fluxes with the increase of the CaO/SiO_2 ratio at certain times. The crystal phases and crystal morphologies formed in different conditions were analysed by X-ray diffraction (XRD), scanning electron microscope (SEM), and X-ray energy dispersive spectroscopy (EDS). Phases formed in the process of the flux crystallisation included $CaSiO_3$, $Ca_2MgSi_2O_7$ and $Ca_{11}Si_4B_2O_{22}$. It revealed that $CaSiO_3$ was the major phase at low CaO/SiO_2 ratio. The amount of $Ca_2MgSi_2O_7$ and $Ca_{11}Si_4B_2O_{22}$ increased with increasing CaO/SiO_2 ratio.

KEY WORDS: fluorine-free mould fluxes; crystallisation behaviour; CaO/SiO_2 mass ratio; hot thermocouple technique.

1. Introduction

Mould fluxes serve indispensable roles in steel continuous casting including strand lubrication, inclusion absorption, heat transfer control from steel strand to copper mould, thermal insulation and oxidation prevention.[1)] Crystallisation behaviour of mould fluxes is a decisive factor in controlling heat transfer rate. The suppression of heat flux can be achieved by applying mould fluxes with high crystallisation tendency and, accordingly, thick crystalline layer[2–6)] due to the scattering effect on thermal radiation at the grain boundaries.[7–10)] Heat transfer is also suppressed by the formation of high thermal resistance pores, cracks and air gaps in the wake of the shrinkage of crystalline layer.[5,11–14)] Currently, most of the commercial mould fluxes contain fluorides, like CaF_2 and NaF, to improve lubricity and control heat transfer rate through the formation of cuspidine ($Ca_4Si_2O_7F_2$).[15–18)] However, the high volatility of fluorides at high temperature brings about serious problems such as health hazards to operators, acid rain and corrosion of submerged entry nozzle and secondary cooling system.[3,4)] The increasing environmental concern for steelmaking industry in recent years makes the development of fluorine-free mould fluxes imperative. The main problem of the development of fluorine-free mould fluxes is the difficulty in controlling heat transfer rate effectively in the absence of cuspidine and finding an appropriate mineralogical phase that could duplicate the performance of cuspidine.

Precipitated phases are mainly determined by the chemical composition of mould fluxes. Wen *et al.*[4)] studied the effect of several components on heat transfer rate of modified $CaO–SiO_2–TiO_2$ based fluorine-free blast furnace slags using a water cooled copper detector. They found that $CaTiO_3$ played a critical role in controlling heat transfer rate. Nakada *et al.*[19)] investigated the influence of TiO_2 on the solidification of fluorine-free mould fluxes using a differential thermal analyser (DTA) and found that the incubation time for the formation of $CaSiTiO_5$ was similar to that for cuspidine in fluorine-containing mould fluxes. Choi *et al.*[20)] indicated that $Ca_2B_2SiO_7$ and $Ca_3Al_{12}BSi_4O_{15}(OH)$ (previously referred as CaB_2SiO_7 and $Ca_3Al_4B_2(SiO_4)_8$, in

* Corresponding author: E-mail: j.q.zhang@unsw.edu.au
DOI: http://dx.doi.org/10.2355/isijinternational.ISIJINT-2015-583

the paper[20]) were formed in the solidification process of fluorine-free mould fluxes whose thermal conductivity was similar to that of commercial fluorine-containing mould fluxes. However, most of the aforementioned studies regarding fluorine-free mould fluxes were conducted in a fixed thermal condition or a mild cooling condition, and few studies have been conducted to reveal their crystallisation behaviour under a transient thermal condition which occurs in an actual continuous casting operation.

In this article, the influence of CaO/SiO_2 mass ratio on the crystallisation behaviour of $CaO–SiO_2–Na_2O–B_2O_3–TiO_2–Al_2O_3–MgO–Li_2O$ mould fluxes was investigated through *in-situ* observation using hot thermocouple technique (HTT) developed by Kashiwaya *et al.*[21,22] Continuous cooling transformation (CCT) diagrams and time-temperature transformation (TTT) diagrams were constructed using single hot thermocouple technique (SHTT). The effects of CaO/SiO_2 ratio and temperature on crystal morphology and precipitated phases were analysed by scanning electron microscopy (SEM) and X-ray diffraction (XRD) respectively. The solidification behaviour under a simulated temperature gradient was studied using double hot thermocouple technique (DHTT). The aim of this work is to develop a fundamental understanding of the effect of CaO/SiO_2 ratio on the phase transformation under various thermal conditions in the fluorine-free system for the design of eco-friendly mould fluxes.

2. Experimental

2.1. Materials Preparation

In the present study, compositions of the mould fluxes were designed on the basis of thermodynamic modelling using FactSage.[23] The mould fluxes were prepared by melting pre-mixed reagent grade $CaCO_3$, SiO_2, Al_2O_3, B_2O_3, Na_2CO_3, TiO_2, MgO and Li_2CO_3 at 1 400°C for 20 min. The melted fluxes were quenched onto a copper plate and then ground into powders. Measured chemical compositions of the prepared amorphous fluxes are listed in **Table 1**. The concentrations of B_2O_3 and Li_2O were determined by inductively coupled plasma (ICP) analysis, and other components were analysed by X-ray fluoroscopy (XRF).

2.2. Experimental Apparatus and Procedure

The experimental study of the crystallisation behaviour of mould fluxes was performed using SHTT for continuous cooling and isothermal experiments, and DHTT for solidification in a simulated temperature gradient. Hot thermocouple technique enables high heating and cooling rates (up to ±30°C/s by the system control and up to ±220°C/s by the manual control), which make it capable of simulating high local cooling rate in infiltration process adjacent to the copper mould.[24] In SHTT, a thermocouple was used to measure and control temperature. The mould flux sample (approximately 10 mg) was mounted on the tip of a B-type thermocouple and heated and cooled in accordance with the programmed temperature profiles. The crystallisation process of mould fluxes was *in-situ* observed and recorded by a video camera.

The CCT and TTT diagrams were constructed using SHTT in continuous cooling and isothermal experiments, respectively. Their temperature profiles are given in **Figs. 1**(a) and 1(b). To construct CCT diagrams, the sample was heated to 1 500°C with the heating rate of 30°C/s and maintained at this temperature for 3 min to homogenise composition and remove bubbles. Then, it was continuously cooled down with different pre-set cooling rates to simulate different cooling paths that mould fluxes may encounter in different regions of the mould during infiltration process.[22] CCT curves were constructed by determining the temperature and time at which the crystallinity of the mould fluxes reached 0.5 vol%. For each cooling rate, three measurements were carried out for the crystallisation temperature and the results were marked as points in corresponding cooling curves.

For the construction of TTT diagrams, the powders were also heated to 1 500°C with the heating rate of 30°C/s and held for 3 min at this temperature. Then it was rapidly quenched to different pre-set temperatures with an initial cooling rate of 220°C/s and held isothermally until a full crystallisation. The onset and end of crystallisation were defined as the times when the crystallinity reached 0.5 and 99 vol%, respectively. The images captured from the recorded videos were processed by a commercial image processing software (ImageJ[25]) for the calculation of crystallinity at certain times. An auxiliary heater was set at 800°C in both measurements to stabilise the natural convection in reaction chamber.[21] Due to the influence of the auxiliary heater and power feedback, the cooling rate gradually dropped from 220°C/s to 0°C/s within a few seconds when the real-time flux temperature was approaching the target temperature. The start point of isothermal treatment was defined as the time at which the tangent to the cooling path and the isothermal temperature line intersected as illustrated in Fig. 1(c).

The crystal morphology of the flux samples at different thermal conditions obtained in isothermal experiments was examined by SEM (Hitachi S3400). As the specimens in the single hot thermocouple were too tiny to examine their phase composition, 5 g amorphous samples were treated at a low temperature (850°C) and a high temperature (1 000°C) respectively, for 20 min in the furnace. The precipitated phases in quenched samples were identified using XRD (PANalytical Empyrean XRD) with Cu-Kα radiation. The scan was conducted in the range of $2\theta = 10°$ to 80° with the step size of 0.026°.

DHTT was employed to investigate the solidification

Table 1. Measured chemical compositions of mould fluxes with varying CaO/SiO_2 ratios (mass%).

Sample	CaO/SiO_2	CaO	SiO_2	Al_2O_3	B_2O_3	Na_2O	TiO_2	MgO	Li_2O
1	0.9	34.7	38.7	3.6	6.9	8.6	4.4	2.3	0.8
2	1.0	36.6	36.6	3.6	6.9	8.7	4.3	2.3	0.9
3	1.1	38.3	34.7	3.7	6.8	8.7	4.2	2.3	0.9
4	1.2	39.9	33.2	3.7	6.8	8.7	4.2	2.2	0.9

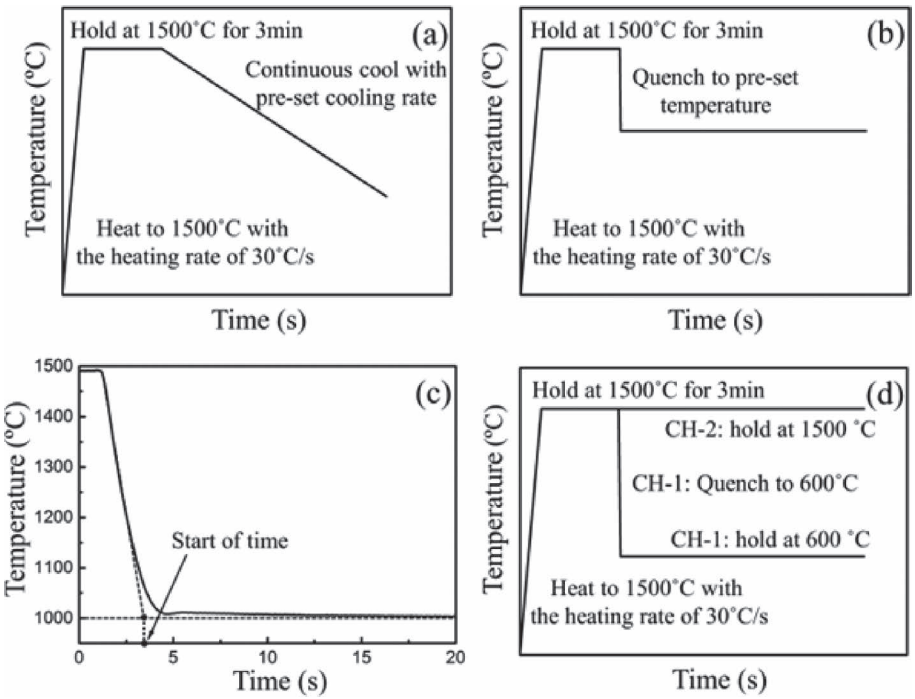

Fig. 1. Schematic temperature profiles in (a) continuous cooling experiment; (b) isothermal experiment; and (c) determination of a start point in the isothermal experiment; and (d) DHTT experiment.

behaviour in a pre-set temperature gradient simulating the thermal field between the cold surface of flux film and strand in meniscus zone. The thickness of flux films in continuous casting operation ranges from 0.5 to 2 mm.[24,26–30] In this study, the distance between two thermocouples was set at 1.5 mm when the flux film was in the liquid state to minimise both temperature interference between two thermocouples and excessive heat loss to the system. High temperature thermocouple was set at 1 500°C to simulate the temperature of liquid flux adjacent to strand in meniscus zone,[26,27] while a low temperature thermocouple was pre-set to simulate the temperature of the cold surface of the flux film. Since the temperature of cold surface of flux film cannot be directly measured, it was calculated using Eq. (1) under one dimensional heat transfer in the steady state.[26,30,31]

$$T_{CS} = T_M + q_T \cdot R_{INT} \quad \text{..... (1)}$$

where T_{CS} is the temperature of cold surface of flux film, T_M is the temperature of hot surface of copper mould, q_T is the heat flux, and R_{INT} is the interfacial thermal resistance. According to the data acquired from the plant operation, T_M ranges from 150 to 300°C which is consistent with the values reported in literatures.[26,27,30] The calculated average q_T is in the range of 0.75 to 2.05 MW/m^2 in plant operation for different steel grades and casting speeds, which accords with the reported values.[24,26,27,30,32] The value of R_{INT} in relevant reports was 0.83 to 8 m^2·K/W.[26,30,32] In this study, the values of T_M, q_T and R_{INT} were assumed to be 200°C, 1 MW/m^2 and 4 m^2·K/W. Therefore, calculated T_{CS} was 600°C, which was applied to the low temperature thermocouple in DHTT experiments. The temperature profile of DHTT experiments is given in Fig. 1(d). The powders in two thermocouples were heated to 1 500°C simultaneously, then intersected and separated to form a liquid flux film between two thermocouples with the length of 1.5 mm. After holding at 1 500°C for 3 min, the low temperature thermocouple (CH-1) was quenched to 600°C while the high temperature thermocouple (CH-2) was kept at 1 500°C. Considering the decreased cooling rate when the temperature of CH-1 was approaching the target, a start point in the DHTT experiments was defined in the same manner as in the SHTT isothermal experiments, as the point in which the tangent to the cooling path of CH-1 and isothermal temperature line (600°C) intersect as illustrated in Fig. 1(c). After the DHTT experiments, the solidified flux films were removed from the apparatus, ground, polished and coated by carbon for SEM analysis. The element analysis of the precipitated phases was done by X-ray energy dispersive spectroscopy (EDS).

3. Results

3.1. Continuous Cooling Experiments

Figures 2(a) to 2(d) show the CCT diagrams of mould fluxes with CaO/SiO$_2$ ratios from 0.9 to 1.2. The crystallisation temperature of the mould fluxes with a certain cooling rate increased with the increase of CaO/SiO$_2$ ratio. For example, the crystallisation temperature of the mould fluxes was 964°C, averaged out from three individual measurements, when CaO/SiO$_2$ = 0.9 and the cooling rate was 1°C/s; it increased to 1 276°C when CaO/SiO$_2$ = 1.2 in cooling with the same rate. A comparison between the CCT diagrams for fluxes with different CaO/SiO$_2$ ratios is illustrated in Fig. 2(e). The crystallisation temperature decreased with increasing cooling rate. For example, the crystallisation temperature of Sample 2 (CaO/SiO$_2$ = 1.0) decreased from 1 095°C when the cooling rate was 0.1°C/s to 932°C when the cooling rate raised to 2°C/s (Fig. 2(b)). As the CaO/SiO$_2$ ratio increased, the critical cooling rate, above which liquid

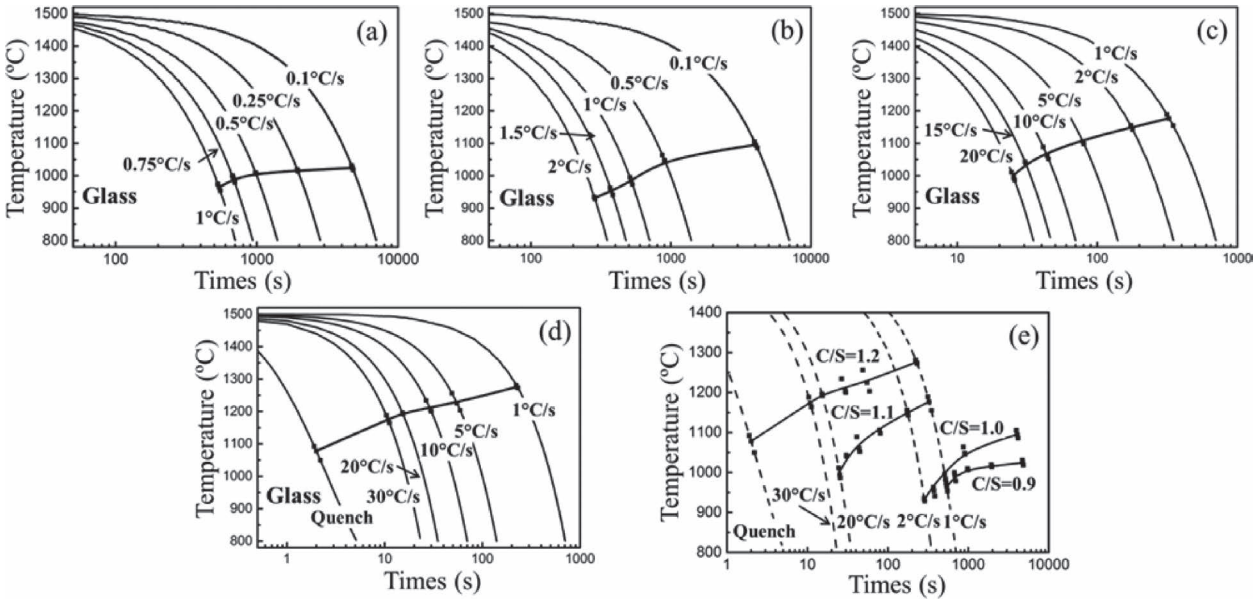

Fig. 2. CCT diagrams of mould fluxes: (a) Sample 1: CaO/SiO_2=0.9; (b) Sample 2: CaO/SiO_2=1.0; (c) Sample 3: CaO/SiO_2=1.1; (d) Sample 4: CaO/SiO_2=1.2; and (e) onset of crystallisation at different CaO/SiO_2.

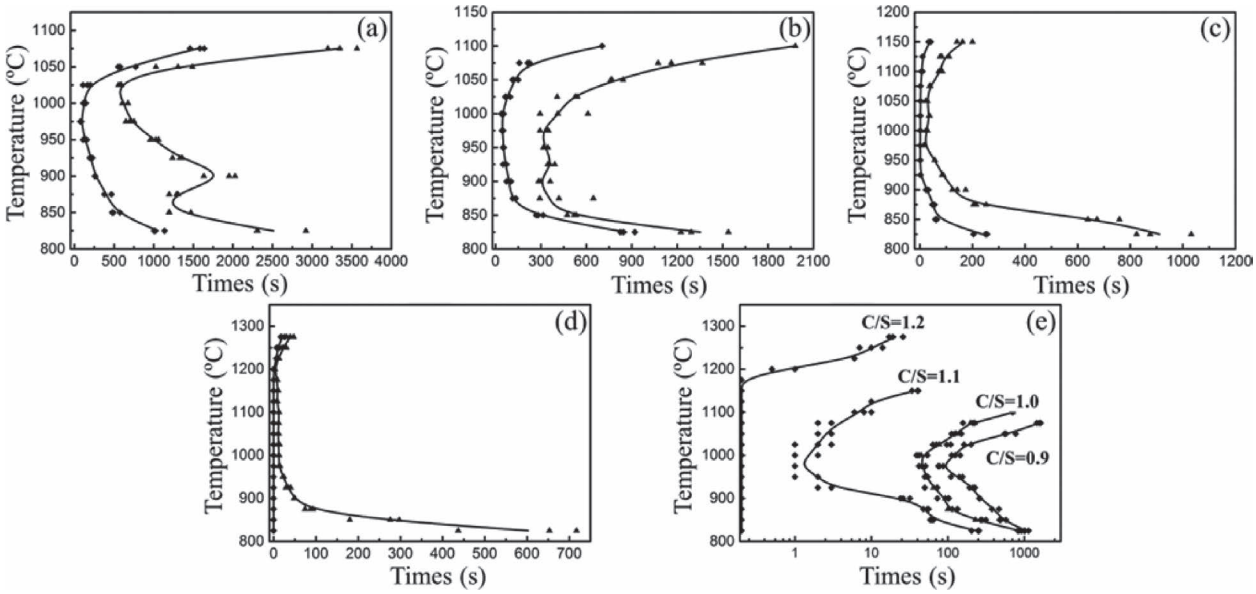

Fig. 3. TTT diagrams of mould fluxes showing the onset (0.5 vol%) and end (95 vol%) of crystallisation: (a) Sample 1: CaO/SiO_2=0.9; (b) Sample 2: CaO/SiO_2=1.0; (c) Sample 3: CaO/SiO_2=1.1; (d) Sample 4: CaO/SiO_2=1.2; and (e) onset of crystallisation at different CaO/SiO_2 ratios.

phase is completely transformed to glass, raised from 1°C/s for CaO/SiO_2 = 0.9, 2°C/s for CaO/SiO_2 = 1.0, 20°C/s for CaO/SiO_2 = 1.1, and further to over 30°C/s for CaO/SiO_2 = 1.2. The cooling rate for quenching of Sample 4 into glass was approximately 150°C/s.

3.2. Isothermal Experiments

TTT diagrams of mould fluxes with different CaO/SiO_2 ratios are presented in **Figs. 3**(a) to 3(d); Fig. 3(e) compares the onsets of crystallisation of mould fluxes with different CaO/SiO_2 ratios. As CaO/SiO_2 ratio increased, the incubation time decreased and the highest crystallisation temperature increased as shown in **Table 2**. It is noteworthy that the mould fluxes with CaO/SiO_2 = 1.2 started crystallisation before it reached isothermal temperature.

Table 2. Shortest incubation time and highest crystallisation temperature of mould fluxes with different CaO/SiO_2 ratios.

CaO/SiO_2 ratio	Shortest $t_{incubation}$ (s)	Highest $T_{crystallisation}$ (°C)
0.9	80	1 075
1.0	53	1 100
1.1	1	1 150
1.2	≈0	1 275

XRD patterns of the flux samples isothermally treated at 850°C and 1 000°C are given in **Fig. 4**. The dominant phase of Sample 1 (CaO/SiO_2 = 0.9) at both 850°C and 1 000°C was $CaSiO_3$. Minor precipitation of $Ca_{11}Si_4B_2O_{22}$ was also detected at both temperatures, while $Ca_2MgSi_2O_7$ was only

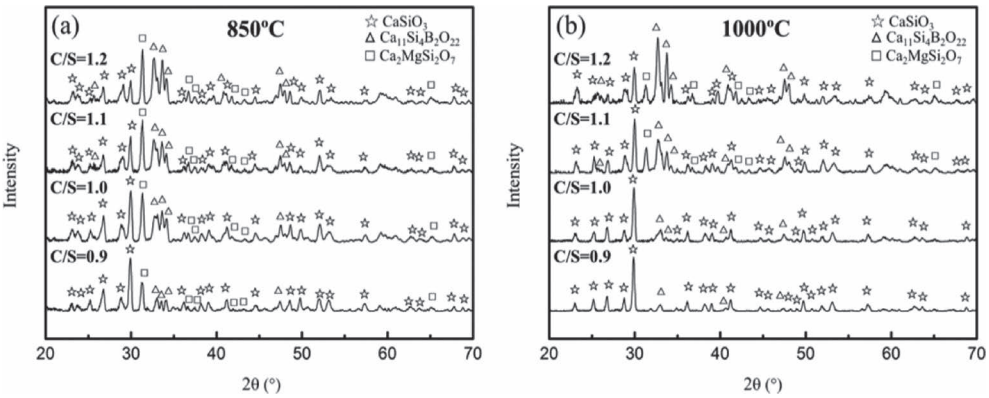

Fig. 4. XRD patterns of samples with different CaO/SiO_2 ratios heat-treated at (a) 850°C, and (b) 1 000°C.

found at 850°C. When CaO/SiO_2 ratio increased to 1.0, the dominant precipitate remained $CaSiO_3$ but the relative amounts of $Ca_{11}Si_4B_2O_{22}$ and $Ca_2MgSi_2O_7$ increased based on the comparison between the heights of main peaks of individual phases. The amount of $Ca_2MgSi_2O_7$ increased significantly at 850°C, exhibiting a similar main peak height to that of $CaSiO_3$. With the further increase of CaO/SiO_2 ratio, the precipitation of $Ca_{11}Si_4B_2O_{22}$ and $Ca_2MgSi_2O_7$ was promoted drastically. $Ca_{11}Si_4B_2O_{22}$ became the dominant phase in the fluxes with the CaO/SiO_2 ratio of 1.2 at 1 000°C, and $Ca_2MgSi_2O_7$ was found to be the dominant phase in the samples with the CaO/SiO_2 ratio of 1.1 and 1.2 at 850°C.

Crystals of different size and shape - fine, columnar and large equiaxed crystals, were observed in samples exposed to different thermal conditions as shown in **Fig. 5**. Columnar crystals were formed in the samples with all CaO/SiO_2 ratios in different temperature ranges, growing from the interface between the thermocouple and flux pool (Fig. 5(a)) to the centre of flux pool. The growth rate of columnar crystals varied significantly with the CaO/SiO_2 ratios. With a high CaO/SiO_2 ratio (Sample 4), columnar crystals could fill up the flux pool within ten seconds after nucleation; while it took more than 8 min to cover the flux pool if the CaO/SiO_2 ratio was low (Sample 1) as shown in **Fig. 6**. A typical microstructure of such columnar crystals is shown in Fig. 5(b). Fine crystals (or "cloud crystals"[33]) with less than 30 μm in diameter, as shown in Figs. 5(c) and 5(d), were more likely to form at low temperature range in the mould fluxes with low CaO/SiO_2 ratio. Further SEM analysis revealed that these fine crystals had a snowflake-like morphology (Fig. 5(d)). The microstructure indicated that they were undeveloped equiaxed crystals. The large equiaxed crystals precipitated at high temperatures in the mould fluxes with high CaO/SiO_2 ratio through the rapid homogeneous nucleation (Fig. 5(e)). The size of large equiaxed crystals was normally over 100 μm as indicated in Fig. 5(f). Primary and secondary dendritic arms formed quickly after nucleation. All of these columnar, tiny and large equiaxed crystals were of dendritic structure.

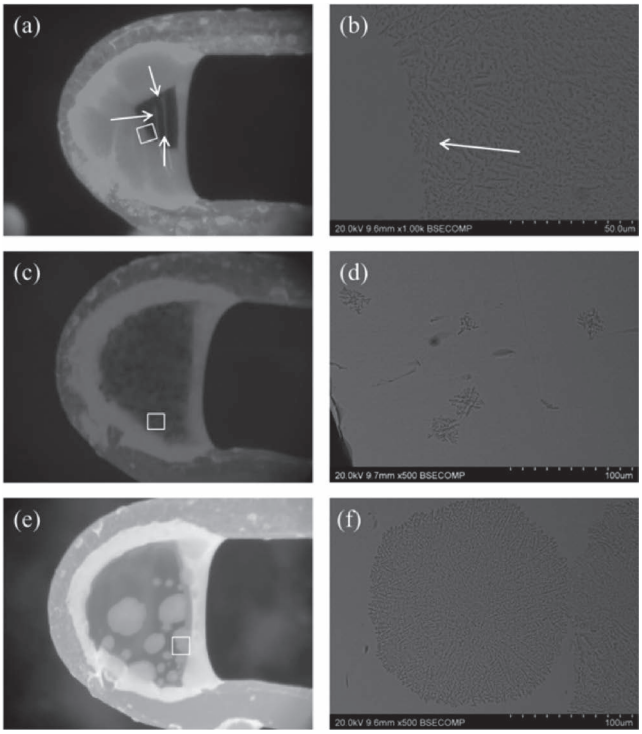

Fig. 5. Crystal morphology and microstructure of mould fluxes in different thermal condition and composition: (a)–(b) Sample 1 at 1 000°C, 376 s; (c)–(d) Sample 1 at 900°C, 1 213 s; and (e)–(f) Sample 4 at 1 225°C, 2 s. Figures (b), (d), (f) are the SEM images of the areas marked by white boxes in Figs. (a), (c) and (e) repectively.

3.3. DHTT Experiments

The crystallisation behaviour of mould fluxes with different CaO/SiO_2 ratios in a simulated thermal field is shown in **Figs. 7** to **10**. In the initial stage, the low temperature thermocouple (CH-1) had been quenched from 1 500°C to 600°C which transformed the flux film attached to the low temperature thermocouple into glassy state, while the high temperature thermocouple (CH-2) remained at 1 500°C. Some small spherical crystals started to precipitate in Sample 1 after 296 s (Fig. 7(a)). Afterward, columnar crystals precipitated on the primarily formed crystals, and propagated to both high temperature and low temperature sides. The centre of the flux film was developed from several primarily precipitated crystals to an apparent crystalline layer during this period as presented in Figs. 7(b) and 7(c). In this process, a small portion of the crystals emerged in the liquid/crystalline interface were moved toward CH-2 and melted in the high temperature region. After 1 019 s, the structure of the film reached a relatively stable state (Fig. 7(d)). The crystallisation behaviour of Sample 2 (CaO/SiO_2 = 1.0) in the same thermal field is shown in Fig. 8. The precipitation

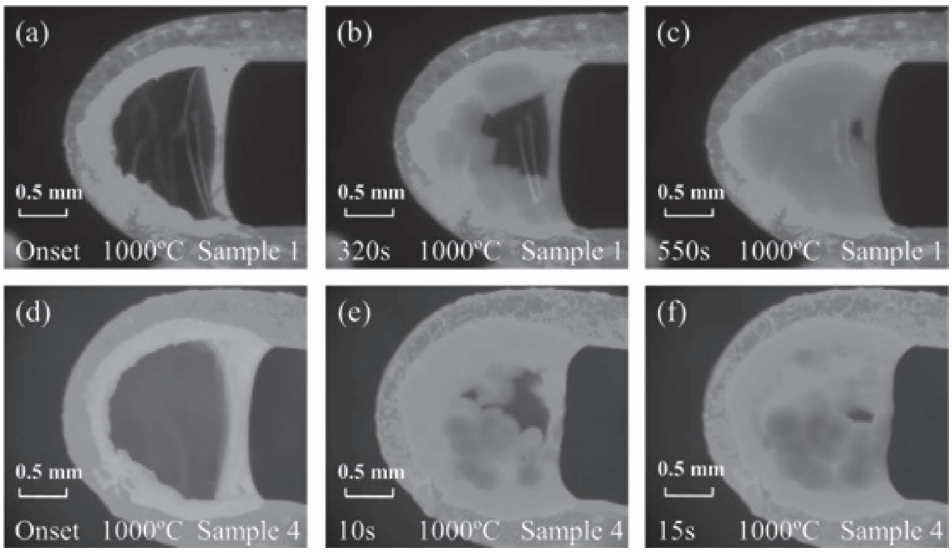

Fig. 6. Columnar crystal growth at 1 000°C in the samples with different CaO/SiO_2 ratios: (a)–(c) Sample 1; and (d)–(f) Sample 4.

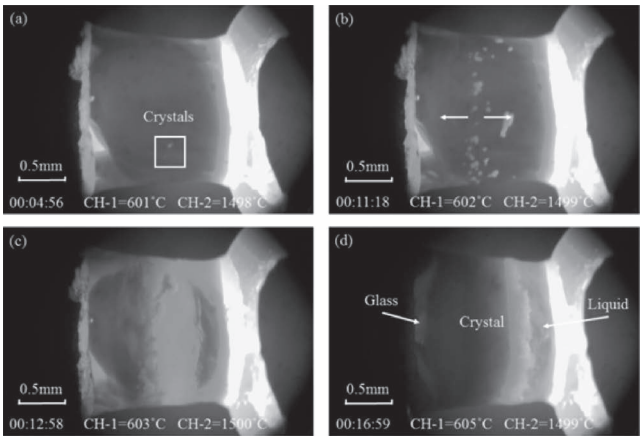

Fig. 7. Crystallisation behaviour of Sample 1 (CaO/SiO_2=0.9) in DHTT experiment at: (a) 296 s; (b) 678 s; (c) 778 s; and (d) 1 019 s.

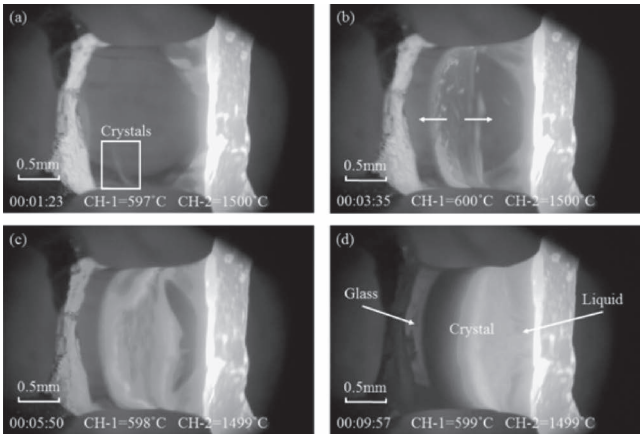

Fig. 8. Crystallisation behaviour of Sample 2 (CaO/SiO_2=1.0) in DHTT experiment at: (a) 83 s; (b) 215 s; (c) 350 s; and (d) 597 s.

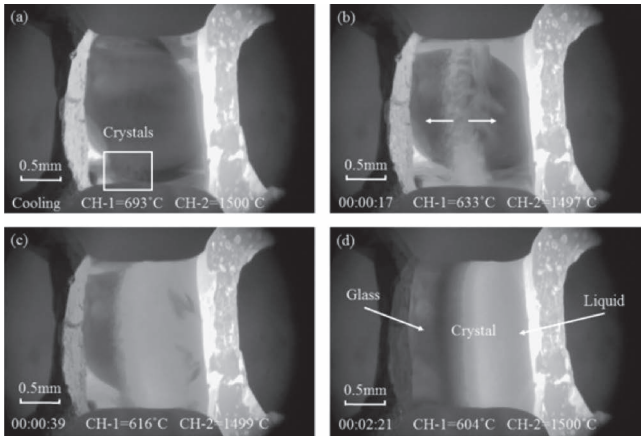

Fig. 9. Crystallisation behaviour of Sample 3 (CaO/SiO_2=1.1) in DHTT experiment during: (a) cooling process; and at (b) 17 s; (c) 39 s; and (d) 141 s.

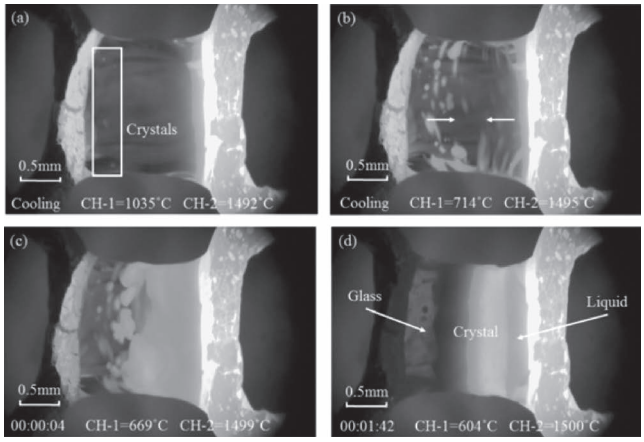

Fig. 10. Crystallisation behaviour of Sample 4 (CaO/SiO_2=1.2) in DHTT experiment during: (a)–(b) cooling process; and at (c) 4 s; and (d) 102 s.

of crystals started after 83 s and achieved a steady state after 597 s, significantly shorter than those in crystallisation of Sample 1. The crystallisation of Sample 3 (CaO/SiO_2 = 1.1, Fig. 9) took place at 693°C in the cooling process of thermocouple CH-1, 2 s before CH-1 reached isothermal stage. Crystals in this flux grew rapidly and formed a clear crystalline layer within 39 s as seen in Fig. 9(c). Noticeable crystallisation process ended after 141 s. Figure 10 shows the crystallisation behaviour of Sample 4 (CaO/SiO_2 = 1.2). Crystallisation started at 1 035°C in the cooling process.

Several individual equiaxed crystals first precipitated in the lower temperature region of the glassy zone then appeared in the higher temperature region. Afterward, a large amount of equiaxed crystals emerged in the liquid zone and rapidly spread over most of the liquid zone (Figs. 10(b) and 10(c)). A distinct crystalline layer was formed within seconds after CH-1 reached isothermal stage (Fig. 10(c)). Crystallisation achieved a stable state after 102 s of isothermal treatment (Fig. 10(d)).

The microstructure of flux films formed in DHTT experiments was analysed using SEM and EDS. The flux film morphologies of Sample 1 and Sample 4 are presented in **Fig. 11**. Two samples all showed a clear three-layer structure. The glassy layer on the left side was the original glassy phase which was not devitrified throughout DHTT experiments; while the glassy layer on the right side was directly quenched from the liquid state (1 500°C) after DHTT experiment. The boundaries between crystalline and original glassy layer were flat, while those between crystalline and liquid layer (glassy layer to the right in the SEM-BSE images) were relatively jagged. In the SEM-BSE image of Sample 1, paralleled needle-shaped crystals were observed on the cold side (crystal 1, Fig. 11(a)) of crystalline layer growing roughly along the heat transfer direction. The main elements determined as Ca, Si and O implied that the phase was $CaSiO_3$ according to their normalised atomic content. On the hot side, the bulk crystals (crystal 2, Fig. 11(a)) growing from the solid crystalline layer in the centre, as observed in the video, were also suggested as $CaSiO_3$ in EDS analysis. The SEM-BSE image of Sample 4 in Fig. 11(b) shows that the crystals (crystal 2, Fig. 11(b)) nucleated and grew independently in the hot zone. They were supposed to be developed from the rapidly-formed equiaxed crystals as observed in isothermal experiments (Fig. 5(e)).

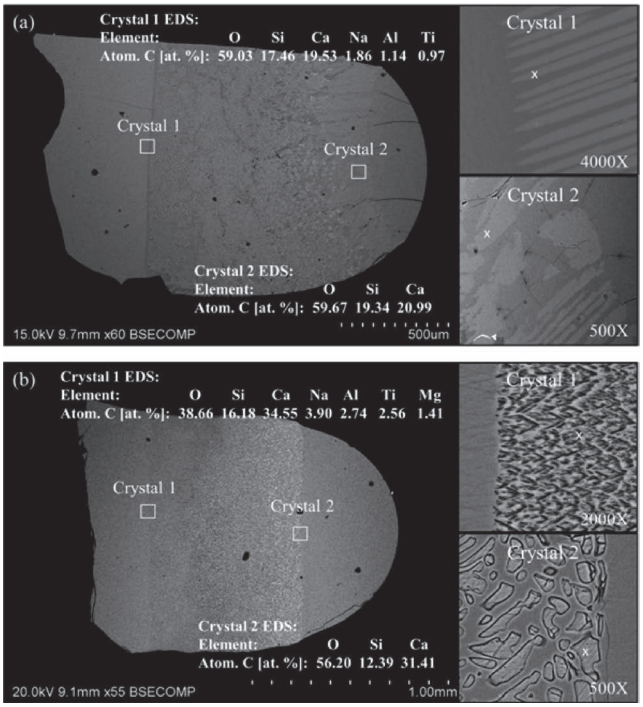

Fig. 11. SEM-BSE image of flux films formed in DHTT experiments: (a) Sample 1 (CaO/SiO_2= 0.9); and (b) Sample 4 (CaO/SiO_2=1.2).

The detected elements were Ca, Si and O. However, the phase is likely to be $Ca_{11}Si_4B_2O_{22}$ according to the Ca/Si ratio and XRD results (boron is too light to be analysed in the EDS package). Information about the elemental composition of the crystals precipitated in the low temperature region (crystal 1, Fig. 11(b)) was insufficient to identify the phase. The mash-like morphology in this area was different from the form of needle-shaped structure in Sample 1.

4. Discussion

Effect of CaO/SiO_2 ratio on crystallisation of mould fluxes studied in this paper is related to the properties of molten fluxes, precipitation of different phases in the process of crystallisation and morphology of precipitated phases.

4.1. Effects of Structure and Properties of Molten Fluxes on Nucleation and Growth of Crystal Phases

The structure of silicate-based flux melts can be expressed as a random network of SiO_4^{4-} tetrahedra. The addition of CaO leads to the formation of non-bridging oxygens (NBOs),[34] and therefore enhances the mobility of the building units and the network modifiers within the melts,[35] affecting the kinetics of crystallisation process. Both the increase of critical cooling rate and the decrease of incubation time with increasing CaO/SiO_2 ratio, as summarised in **Fig. 12**, suggest that kinetic barriers for the formation of detectable crystal clusters were reduced. Nucleation rate I is expressed using Eq. (2):[36]

$$I = A\exp\left(-\frac{W^* + \Delta G_D}{kT}\right) \quad \text{..... (2)}$$

where A is the pre-exponential factor, W^* is the thermodynamic free energy barrier for nucleation or net energy change for the critical nucleus, ΔG_D is the kinetic free energy barrier for nucleation, k is the Boltzmann constant, and T is the absolute temperature. Equation (2) can be further combined with Stokes-Einstein relation:

$$I = \left(\frac{Ah}{3\pi\lambda^3\eta}\right)\exp\left(-\frac{W^*}{kT}\right) \quad \text{..... (3)}$$

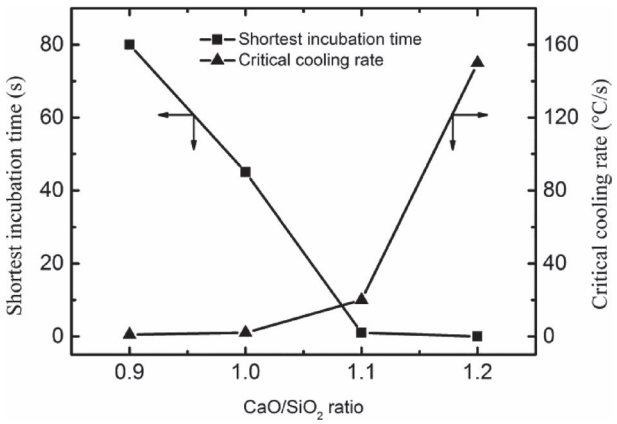

Fig. 12. The relationship between critical cooling rate, shortest incubation time and CaO/SiO_2 ratio of tested mould fluxes.

where h is Planck constant, λ represents the atomic jump distance, and η is the viscosity. Similar to the expression of nucleation rate, crystal growth rate U is given by the following equation:[36)]

$$U = \frac{kT}{3\pi a_a^2 \eta}\left[1-\exp\left(\frac{\Delta G}{kT}\right)\right] \quad \ldots\ldots\ldots\ldots\ldots (4)$$

where a_a is the interatomic separation distance, ΔG is the thermodynamic barrier for crystal growth. With the addition of CaO, the increasing ion mobility in depolymerised silicate network results in a decreasing viscosity of flux melts (η). For the nucleation and crystal growth in identical thermodynamic condition, the high diffusion coefficient of the melts with low initial viscosity reduces the kinetic barrier for both nucleation and subsequent crystal growth. This is also consistent with the tendency in fluorine-containing mould fluxes.[5)]

For the mould fluxes with a given chemical composition, different cooling paths in continuous cooling experiments could affect crystallisation behaviour. The high cooling rate leads to the rapid increase of viscosity of melt as temperature descends. This phenomenon also increases the kinetic barrier and requires higher undercooling to initiate crystallisation, which explains the decrease of the crystallisation temperature with the increase of cooling rate.

Based on the results of continuous cooling and isothermal experiments, Samples 1 (CaO/SiO_2 = 0.9) and 2 (CaO/SiO_2 = 1.0) are likely to freeze into glassy phase once they meet the copper mould due to the high local cooling rate (20°C/s)[37)] in an actual continuous casting operation. Thick glassy and liquid layers are normally associated with the mould fluxes with low CaO/SiO_2 ratio, which would improve the lubricity of flux films. Meanwhile, Samples 3 (CaO/SiO_2 = 1.1) and 4 (CaO/SiO_2 = 1.2) form crystalline phase directly from liquid state due to their high critical cooling rates (20 and over 30°C/s, respectively). Thick crystalline layer is the signature of such mould fluxes with high CaO/SiO_2 ratio, which would enhance the thermal resistance of flux films. Furthermore, the shortest incubation time in isothermal experiments could be used to empirically determine if a type of mould fluxes can be applied to plant casting. According to our preliminary works on commercial mould fluxes and literatures,[31,38)] the shortest incubation time of mould fluxes for medium carbon steel casting, is normally shorter than 1 s;[31)] while that for low carbon steel casting is usually longer than 15 s[31,38)] as indicated in **Fig. 13**. The comparison of their incubation times indicates that the mould fluxes with high CaO/SiO_2 ratio may be more suitable for cracking-sensitive steel casting, *e.g.* medium carbon steel, while those with low CaO/SiO_2 ratio are favoured in sticking-sensitive steel casting, *e.g.* low carbon steel. By adjusting the CaO/SiO_2 ratio, it is possible to duplicate the crystallisation behaviour of fluorine-containing mould fluxes in compliance with different casting conditions.

4.2. Precipitated Phases in the Process of Flux Solidification

Precipitated phases during solidification process depend upon the composition of mould fluxes and thermal conditions (Fig. 4). The TTT diagrams for the end of crystallisation exhibit more than one nose (Fig. 3) which is characteristic for precipitation of different phases. The equilibrium phase diagram of the designed mould flux system calculated using FactSage Thermodynamic Calculation Package (version 6.4) for varying CaO and SiO_2 concentrations is shown in **Fig. 14**. Zero phase fraction (ZPF) curves of $CaSiO_3$, $Ca_3MgSi_2O_8$ and $Ca_{11}Si_4B_2O_{22}$ highlighted in the phase diagram show the formation boundaries of these phases. As can be seen, $CaSiO_3$ is favoured to precipitate at low concentration of CaO, while $Ca_{11}Si_4B_2O_{22}$ and $Ca_3MgSi_2O_8$ form at relatively high concentration of CaO. XRD analysis (Fig. 4) confirmed that $CaSiO_3$ was the major phase at low CaO/SiO_2 ratio and the precipitation of $Ca_{11}Si_4B_2O_{22}$, a partial solid solution of B_2O_3 in Ca_2SiO_4, was promoted at high temperature with high CaO/SiO_2 ratio, which is in accordance with the thermodynamic expectation. Wei *et al.*[39)] in their study of low fluorine-containing mould fluxes suggested that $Ca_{11}Si_4B_2O_{22}$ was a possible substitution for cuspidine due to their similar melting properties. The melting temperature of $Ca_{11}Si_4B_2O_{22}$ is 1 420°C[40)] which is close to the melting temperature of cuspidine (1 407°C[39,41)]). From the perspective of crystallisation, formation of $Ca_{11}Si_4B_2O_{22}$ with rapid nucleation and growth can be effective in the casting of cracking-sensitive steel as a rapid crystallisation in flux film could lead to the stable mild cooling effect on the strand;[42)] while mould fluxes with low CaO/SiO_2 ratio would be more suitable for sticking-sensitive steel casting in terms of its low crystallisation tendency resulting in a better lubricity for strand. An Mg-containing phase, $Ca_3MgSi_2O_8$, predicted by the thermodynamic calculation is slightly different from $Ca_2MgSi_2O_7$ detected by XRD analysis. It should be noticed that the solidification of mould fluxes in SHTT and DHTT experiments occurred under non-equilibrium conditions. Therefore, some discrepancies between calculated phases and results of XRD analysis are not unexpected.

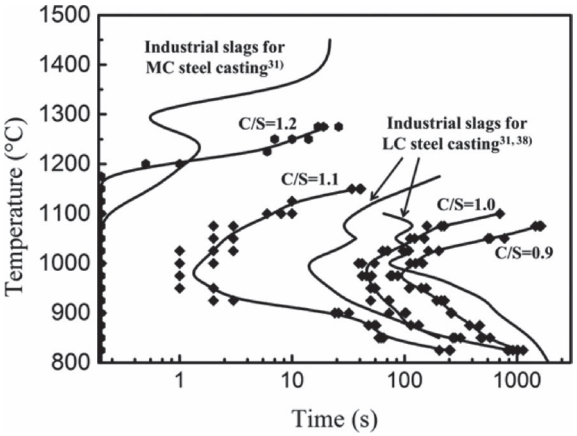

Fig. 13. Comparison of onset of crystallisation in TTT diagrams of fluoride-free mould fluxes and fluoride-containing industrial mould fluxes.

4.3. Crystal Morphology and Microstructure of Mould Fluxes

The nucleation and growth rate of columnar crystals mainly rely on the chemical composition of mould fluxes as illustrated in Fig. 6. The addition of CaO breaks Si–O–Si bond and accelerates the mobility of the ions, resulting in

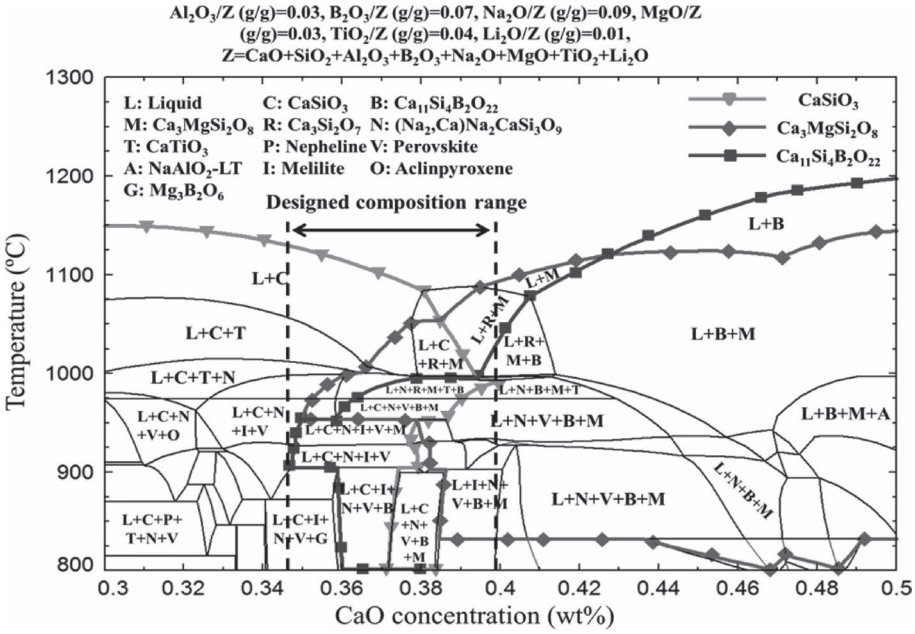

Fig. 14. Phase diagram of designed mould fluxes calculated using FactSage (Version 6.4).

higher nucleation and growth rates as indicated by Eqs. (3) and (4). As the thermal condition in single hot thermocouple was more complicated than one dimensional condition, some secondary dendritic arms could also be observed (Fig. 5(b)). However, the growth direction of columnar crystals was normally from the interface to the centre of flux pool. The growth of equiaxed crystals is considered to be prone to both thermal condition and chemical composition. The crystal size of tiny equiaxed crystals (<30 μm) shown in Fig. 5(d) is limited by the low mobility of the ions resulting from the high viscosity of fluxes and degree of polymerisation at low temperature. Similar grain size and morphology were reported by Mizuno *et al.* in their low temperature heat-treated industrial mould fluxes.[43] Meanwhile, the high undercooling promoted the nucleation rate leading to a large number of nuclei and a cloud-like flux pool. The density of the crystals in SHTT image (Fig. 5(c)) could be higher than that measured in the SEM-BSE image (Fig. 5(d)) since the density of crystals in SHTT photograph counted all the crystals at different depths but SEM-BSE image can only provide the microstructure of the polished layer. Unlike the case of tiny equiaxed crystals, short incubation time and high growth rate are associated with the large equiaxed crystals, implying a high crystallisation tendency. They formed at relatively high temperature and CaO/SiO_2 ratio where low viscosity would take effect. The large difference between their crystallisation features might also attribute to their different crystalline phases with different thermodynamic barrier for nucleation and crystal growth. The similar phenomena were also observed in some reports[18,33,42] related to the crystallisation of fluorine-containing mould fluxes.

4.4. Mould Flux in Simulated Thermal Field

Glassy, crystalline and liquid layers were formed in all the samples under the simulated thermal condition in double hot thermocouple experiments, which is consistent with a three-layer structure of flux films between copper mould and strand in continuous casting.[28,42] According to the time that crystals incubated and grew to a steady three-layer state, Sample 4 had the highest crystallisation tendency which is consistent with what is suggested by CCT and TTT diagrams. Mould fluxes with low CaO/SiO_2 ratio (Samples 1 and 2) are likely to freeze into the glassy phase during the infiltration process near the meniscus zone. Then, a part of this glassy phase devitrifies. This is consistent with the case in the casting of sticking-sensitive grade steel. The mould fluxes with high CaO/SiO_2 ratio are possible to crystallise directly from the liquid state during infiltration process. Afterward, crystals will also emerge easily from both devitrification in the glassy region and direct precipitation in liquid region. This situation is observed frequently in the casting of cracking-sensitive grade steel.[26] It was quite common in the DHTT experiments that some weak parts of the crystalline layer could be broken and moved toward the high temperature region. This phenomenon resulted from Marangoni convection flow caused by the surface tension gradient throughout the flux film.[31]

Different phases and crystal morphologies were observed in the microstructure analysis of the flux film (Fig. 11). In the DHTT experiments, the thermal field was close to one-dimensional. The crystals were able to grow along this heat transfer direction. This phenomenon becomes more significant in one-dimensional crystals growth in the systems with low crystallisation tendency.[44] In the crystallisation of Sample 1 with the lowest crystallisation tendency, the needle-shaped crystals which grew along the heat transfer direction at low temperature were observed. However, in the SHTT experiments, the crystals growth in other directions was less restricted, and the needle-shaped crystals were not observed. It is noteworthy that the liquid layer of Sample 1 displayed in SEM-BSE image was slightly thinner than that of Sample 4, which can be explained by relatively higher mobility of the precipitated equiaxed crystals in Sample 4 in the high temperature region. These isolated crystals were easily driven by the Marangoni convection flow and melted in the high temperature zone which was observed in the video of DHTT experiment. However, the bulk crystals growing from the centre to high temperature side in Sample

1 (see Fig. 11(a)) seem to have a stronger connection with the central crystalline layer, which makes them less affected by Marangoni flow.

5. Conclusions

The crystallisation behaviour of mould fluxes of the $CaO–SiO_2–Na_2O–B_2O_3–TiO_2–Al_2O_3–MgO–Li_2O$ system with varying CaO/SiO_2 mass ratio was investigated using SHTT, DHTT, XRD, SEM and EDS. The major findings of this study are summarised below:

(1) It follows from the CCT diagrams that the critical cooling rate for crystallisation of mould fluxes increased with increasing CaO/SiO_2 ratio, especially when CaO/SiO_2 was beyond 1.1. The incubation time at a given temperature decreased as CaO/SiO_2 ratio increased as indicated by the TTT diagrams. The increase of CaO/SiO_2 ratio enhanced the crystallisation tendency of mould fluxes.

(2) Major phases detected by XRD analysis of quenched fluxes included $CaSiO_3$, $Ca_{11}Si_4B_2O_{22}$ and $Ca_2MgSi_2O_7$. $CaSiO_3$ was the major precipitated phase in the mould fluxes with low CaO/SiO_2 ratio. The amount of $Ca_2MgSi_2O_7$ and $Ca_{11}Si_4B_2O_{22}$ increased with increasing CaO/SiO_2 ratio, becoming the main phase at 850°C and 1 000°C, respectively at high values of CaO/SiO_2. The precipitation of $CaSiO_3$ and $Ca_{11}Si_4B_2O_{22}$ was in agreement with results of thermodynamic calculation, whereas the calculated phase diagram included $Ca_3MgSi_2O_7$ instead of $Ca_2MgSi_2O_7$ which was observed in the XRD patterns.

(3) Crystal morphology depended on both thermal condition in solidification and chemical composition of mould fluxes. Columnar crystals were formed in samples with all CaO/SiO_2 ratios through heterogeneous nucleation; fine crystals were more likely to form at low temperature range in the mould fluxes with low CaO/SiO_2 ratio; large equiaxed crystals favoured to precipitate in high temperature range in the mould fluxes with high CaO/SiO_2 ratio through rapid homogeneous nucleation.

(4) DHTT experiments simulated the crystallisation behaviour in the interface between steel strand and copper mould, which showed that all the samples exhibited a clear three layer structure – glassy layer, crystalline layer, liquid layer, under the simulated thermal condition. Different crystal morphologies were found in different temperature regions of flux film.

Acknowledgements

Financial support by Baosteel through the Baosteel-Australia Joint Research Centre, Abel Metal Services, and Australian Research Council (ARC Linkage Project LP130100773) is highly acknowledged. Technical support for FactSage calculation by Prof Youn-Bae Kang, Pohang University of Science and Technology (POSTECH), is gratefully acknowledged.

REFERENCES

1) K. Mills and A. Fox: *ISIJ Int.*, **43** (2003), 1479.
2) M. Kawamoto, Y. Tsukaguchi, N. Nishida, T. Kanazawa and S. Hiraki: *ISIJ Int.*, **37** (1997), 134.
3) B. Lu, W. Wang, J. Li, H. Zhao and D. Huang: *Metall. Mater. Trans. B*, **44** (2013), 365.
4) G. Wen, S. Sridhar, P. Tang, X. Qi and Y. Liu: *ISIJ Int.*, **47** (2007), 1117.
5) K. Gu, W. Wang, L. Zhou, F. Ma and D. Huang: *Metall. Mater. Trans. B*, **43** (2012), 937.
6) W. Wang, K. Gu, L. Zhou, F. Ma, I. Sohn, D. J. Min, H. Matsuura and F. Tsukihashi: *ISIJ Int.*, **51** (2011), 1838.
7) S. Ozawa, M. Susa, T. Goto, R. Endo and K. Mills: *ISIJ Int.*, **46** (2006), 413.
8) M. Susa, K. Mills, M. Richardson, R. Taylor and D. Stewart: *Ironmaking Steelmaking*, **21** (1994), 279.
9) W. Wang, L. Zhou and G. Kezhuan: *Met. Mater. Int.*, **16** (2010), 913.
10) W. Wang and A. Cramb: *Steel Res. Int.*, **81** (2010), 446.
11) J. Bothma and P. Pistorius: *Ironmaking Steelmaking*, **34** (2007), 513.
12) C. Orrling, A. Cramb, A. Tilliander and Y. Kashiwaya: *Iron Steelmaker*, **27** (2000), 53.
13) J. Cho, H. Shibata, T. Emi and M. Suzuki: *ISIJ Int.*, **38** (1998), 440.
14) K. Tsutsumi, T. Nagasaka and M. Hino: *ISIJ Int.*, **39** (1999), 1150.
15) M. Hanao, M. Kawamoto, M. Hara, T. Murakami, H. Kikuchi and K. Hanazaki: *Tetsu-to-Hagané*, **88** (2002), 23.
16) J. W. Cho and H. Shibata: *J. Non-Cryst. Solids*, **282** (2001), 110.
17) L. Zhou, W. Wang, F. Ma, J. Li, J. Wei, H. Matsuura and F. Tsukihashi: *Metall. Mater. Trans. B*, **43** (2012), 354.
18) J. Li, W. Wang, J. Wei, D. Huang and H. Matsuura: *ISIJ Int.*, **52** (2012), 2220.
19) H. Nakada and K. Nagata: *ISIJ Int.*, **46** (2006), 441.
20) S.-Y. Choi, D.-H. Lee, D.-W. Shin, S.-Y. Choi, J.-W. Cho and J.-M. Park: *J. Non-Cryst. Solids*, **345** (2004), 157.
21) Y. Kashiwaya, C. E. Cicutti, A. W. Cramb and K. Ishii: *ISIJ Int.*, **38** (1998), 348.
22) Y. Kashiwaya, C. E. Cicutti and A. W. Cramb: *ISIJ Int.*, **38** (1998), 357.
23) Y. Cui, L. Wang, J. Yang, J. Zhang, Y. Sasaki and O. Ostrovski: *Steel Res. Int.*, **86** (2015), 662.
24) Y. Meng and B. G. Thomas: *Metall. Mater. Trans. B*, **34** (2003), 707.
25) C. A. Schneider, W. S. Rasband, K. W. Eliceiri, J. Schindelin, I. Arganda-Carreras, E. Frise, V. Kaynig, M. Longair, T. Pietzsch and S. Preibisch: *Nat. Methods*, **9** (2012), 671.
26) Y. Meng and B. G. Thomas: *ISIJ Int.*, **46** (2006), 660.
27) Y. Meng and B. G. Thomas: *Metall. Mater. Trans. B*, **34** (2003), 685.
28) M. Hanao and M. Kawamoto: *ISIJ Int.*, **48** (2008), 180.
29) Y. Kashiwaya and K. Ishii: *ISIJ Int.*, **42** (2002), 71.
30) A. Yamauchi, K. Sorimachi, T. Sakuraya and T. Fujii: *ISIJ Int.*, **33** (1993), 140.
31) L. Zhou, W. Wang, D. Huang, J. Wei and J. Li: *Metall. Mater. Trans. B*, **43** (2012), 925.
32) P. E. Ramirez-Lopez, P. D. Lee, K. C. Mills and B. Santillana: *ISIJ Int.*, **50** (2010), 1797.
33) A. W. Cramb: *ISIJ Int.*, **54** (2014), 2665.
34) A. Dietzel: *Z. Elektrochem. Angew. Phys. Chemi.*, **48** (1942), 9.
35) W. Vogel: Glass Chemistry, Springer-Verlag, Berlin, (2012), 46.
36) J. E. Shelby: Introduction to Glass Science and Technology, Royal Society of Chemistry, Cambridge, UK, (2005), 14.
37) B. Ho: Master thesis, University of Illinois at Urbana-Champaign, (1992).
38) J. Yang, Y. Cui, L. Wang, Y. Sasaki, J. Zhang, O. Ostrovski and Y. Kashiwaya: *Steel Res. Int.*, **86** (2015), 636.
39) J. Wei, W. Wang, L. Zhou, D. Huang, H. Zhao and F. Ma: *Metall. Mater. Trans. B*, **45** (2013), 643.
40) J. Fletcher and F. Glasser: *J. Mater. Sci.*, **28** (1993), 2677.
41) T. Watanabe, H. Fukuyama, K. Nagata and M. Susa: *Metall. Mater. Trans. B*, **31** (2000), 1273.
42) M. Hanao, M. Kawamoto and T. Watanabe: *ISIJ Int.*, **44** (2004), 827.
43) H. Mizuno, H. Esaka, K. Shinozuka and M. Tamura: *ISIJ Int.*, **48** (2008), 277.
44) J. W. Christian: The Theory of Transformations in Metals and Alloys, Pergamon, London, (2002), 491.